Supporting Information

Hybridized Local and Charge Transfer Dendrimers with Nearly Unity Exciton Utilization Enabling High Efficiency Solution-Processed Hyperfluorescent OLEDs

Yixiao Yin,[a+] Songkun Zeng,[a+] Chen Xiao,[a] Peng Fan,[a] Dong Jin Shin,[b] Dong Jin Shin[b], Ki Ju Kim,[d] Hyewon Nam,[d] Qian Ma,[c] Huili Ma,[c] Weiguo Zhu,[a] Taekyung Kim*,[d,e] Jun Yeob Lee*,[b,f] Yafei Wang*[a]*

Contents

Photophysical equations (TADF process)

$$k_{prompt} = \frac{1}{\tau_{prompt}} \quad (1)$$

$$k_{delayed} = \frac{1}{\tau_{delayed}} \quad (2)$$

$$k_{ISC} = \frac{1 - \phi_{prompt}}{k_{prompt}} \quad (3)$$

$$k_{rISC} = \frac{k_{prompt} k_{delayed} \phi_{prompt}}{k_{ISC} \phi_{prompt}} \quad (4)$$

Where τ_{prompt} and $\tau_{delayed}$ are the lifetime of prompt and delayed components. ϕ_{prompt} and $\phi_{delayed}$ represent the proportion of prompt and delayed components k_{prompt}, $k_{delayed}$, k_{ISC} and k_{rISC} are the rates constant of prompt fluorescence, delayed fluorescence, intersystem crossing and reverse intersystem crossing.

Photophysical equations (hot exciton process)

$$R_{prompt} = \frac{\tau_{prompt} A_1}{\tau_{prompt} A_1 + \tau_{delayed} A_2} \quad (5)$$

$$R_{delayed} = \frac{\tau_{delayed} A_2}{\tau_{prompt} A_1 + \tau_{delayed} A_2} \quad (6)$$

$$\phi_{prompt} = \phi_{PL} R_{prompt} \quad (7)$$

$$\phi_{delayed} = \phi_{PL} R_{delayed} \quad (8)$$

$$k_F = \frac{\phi_{prompt}}{\tau_{prompt}} \quad (9)$$

$$k_{nr} = \frac{k_F}{\phi_{PL}} - k_F \quad (10)$$

$$k_{ISC} = \frac{k_F}{\phi_{prompt}} - k_F - k_{nr} \quad (11)$$

$$k_{prompt} = \frac{1}{\tau_{prompt}} \quad (12)$$

$$k_{delayed} = \frac{1}{\tau_{delayed}} \quad (13)$$

$$k_{rISC} = \frac{k_{prompt} k_{delayed} \phi_{delayed}}{k_{ISC} \phi_{prompt}} \quad (14)$$

A_1 and A_2 are the pre-exponential amplitudes for τ_{prompt} and $\tau_{delayed}$. k_F, k_{nr}, k_{ISC}, and k_{rISC} are the rates of fluorescence decay, nonradiative processes, high-lying intersystem crossing, and high-lying reverse intersystem crossing.

The TTA model

$$I_{DF} \propto \left(\gamma_{TT} t + \frac{1}{[T(0)]}\right)^{-2} \quad (15)$$

The Lippert-Mataga model

The Lippert-Mataga model is estimated according to equation 1 as below.

$$hc(v_a - v_f) = hc\left(v_a^0 - v_f^0\right) + \frac{2(\mu_e - \mu_g)^2}{a_0^3} f(\varepsilon,n) \quad (16)$$

According to the equation 1, we got

$$\mu_e = \mu_g + \left\{\frac{hca_0^3}{2} \cdot \left[\frac{d(v_a - v_f)}{df(\varepsilon,n)}\right]\right\}^{1/2} \quad (17)$$

Where μ_e is the dipole moment of excited state, μ_g is the dipole moment of ground state, h is the Plank constant, c is the light speed in vacuum, $v_a - v_f$ is the Stokes shift, a_0 is the solvent Onsager cavity radius and $f(\varepsilon,n)$ is the orientational polarizability of solvents. a_0 and $f(\varepsilon,n)$ can be calculated as follows:

$$a_0 = \sqrt[3]{\frac{3M}{4N\pi d}} \quad (18)$$

Where N is the Avogadro number, M is the molecular weight and d is the density.

$$f(\varepsilon,n) = [\frac{\varepsilon - 1}{2\varepsilon + 1} - \frac{n^2 - 1}{2n^2 + 1}] \quad (19)$$

Where ε is the solvent dielectric constant and n is the solvent refractive index.

Fermi's golden rule

$$k_{rISC} \propto \left| \frac{\langle \psi_{S_m} | \hat{H}_{SO} | \psi_{T_n} \rangle}{\Delta E_{S_m - T_n}} \right| \quad (20)$$

$\langle \psi_{S_m} | \hat{H}_{SO} | \psi_{T_n} \rangle$ is the SOC matrix element between T_n and S_m, $\Delta E_{S_m - T_n}$ is the energy gap between T_n and S_m.

Energy transfer equations

$$R_0^6 = \frac{9000(ln10)\kappa^2 \phi_{pl}}{128\pi^5 N_A n^4} \int_0^\infty F_h(\lambda)\varepsilon_g(\lambda)\lambda^4 d\lambda \quad (21)$$

$$R_{hg} = \left(N_g \times \frac{4\pi}{3} \right)^{-\frac{1}{3}} \quad (22)$$

$$K_{FRET} = \frac{1}{\tau_h}\left(\frac{R_0}{R_{hg}}\right)^6 \quad (23)$$

$$N_g = \frac{\beta \times \rho \times N_A}{M_C} \quad (24)$$

Where R_0 is the distance of FRET radius, $\int_0^\infty F_h(\lambda)\varepsilon_g(\lambda)\lambda^4 d\lambda$ is the spectral overlap integral, N_A is the Avogadro's number, λ is the wavelength, n is the refractive index of the medium, κ^2 is an orientation factor, ϕ_{pl} is the quantum yield, R_{hg} is the radius of the host and guest, β is the fraction of guest in the film, ρ is the density of the film, M_C is the molecular weight of guest.

$$K_{DET} = KJexp[-2R_{hg}/r_h + r_g] \quad (25)$$

Where K is a parameter relative to the specific orbital interactions, J is the spectral overlap integral, r_h and r_g are the Vander Waals radius of the host and the guest.

Reagents and materials

Unless other noted, all reagents used in the experiments were purchased from commercial sources without further purification. For column chromatography, silica gel with 200 ~ 300 mesh was used.

Measurements

Nuclear magnetic resonance (^{1}H NMR and ^{13}C NMR) spectra were obtained on a Bruker 300/400/500 MHz spectrometer (in $CDCl_3$ with internal standard of tetramethyl silane). Resonance patterns were reported with the notation s (singlet), d (double), t (triplet), q (quartet) and m (multiple). Mass spectra were recorded by MALDI-TOF MS (Bruker Autoflex, CH_2Cl_2) and LC-MS (SQD 2, CH_3CN). UV-visible absorption spectra were recorded on a Shimadzu UV-1750. Steady-state fluorescence/phosphorescence spectra PL spectra were carried out by using Edinburgh FLS1000 fluorescence spectrophotometer. The lifetime spectra were carried out on Edinburgh FLSP1000 fluorescence spectrophotometer

equipped with a xenon arc lamp (Xe900) or microsecond flash-lamp (μF900). Photoluminescence quantum efficiency was determined by using a Horiba Scientific Fluorolog-3 spectrofluorometer equipped with a Horiba Scientific Quanta-φ calibrated integrating sphere. Cyclic Voltammetry (CV) was performed on a CHI660e voltammetric analyzer Instruments. Individual samples were respectively dissolved in $CHCl_3$ and degassed with nitrogen gas for 20 minutes before the test. 0.1M tetrabutylammonium hexafluorophosphate ($[nBu_4N]PF_6$) acts as the supporting electrolyte, while a gold, a platinum and a 3.0 M $Ag/AgNO_3$ electrodes play the role of working, counter and reference electrode, respectively. For mageto-electroluminescence (MEL) measurements, magnetic field was applied with permanent magnet pair moving on the rail. Voltage was applied using a source meter (Keithley 2400), and light intensity was detected by photomultiplier tube (Hamamatsu, H13661) and collected as EL data using a multimeter (Keysight, 34465a). The OLED devices were mounted between two magnets and the magets moved twoard the device at a speed of 10 mm/s through motor motion to a point where the central magnetic field reaches a maximum of 250 mT. The magnetic field at the center of the device was pre-calibrated as a function of the distance between the magnets. The MEL data were obtained according to the formula as follows $MEL= [I(B) - I(B_0)]/I(B_0)$.

Devices fabrications

The prepatterned ITO substrates were cleaned with isopropyl alcohol, acetone, detergent and deionized water in an ultrasonic bath. Afterwards, the substrates were dried in the oven at 80 °C. After UV-ozone treatment for 15 min, the PEDOT:PSS layer was directly spin-coated on the ITO substrate as the hole-injecting layer, and then the substrate was transferred into the glovebox filled with N_2 and annealed at 150 °C for 15 min. Then, PVK was spin-coated as hole-transporting layer and annealed at 120 °C for 15 min. The emissive layer was also prepared by spin-coating directly on the hole- transporting layer. Finally, DPEPO as the electron-transporting material, TmPyPB as the electron-transporting material, LiF as the

electron- injecting material and aluminum as the cathode material were consecutively thermally evaporated onto the emissive layer in a vacuum chamber of 1 × 10-4 Pa. The emissive layer of no-doped OLEDs and host-sensitized OLEDs annealed at 80 °C for 15 min. The emissive layer of doped OLEDs annealed at 60 °C for 30 min. In addition, the doped OLEDs doesn't require hole-transporting layer and electron-transporting layer. The experimental data were obtained using a PHOTORESEARCH Spectra Scan PR735 photometer and a KEITHLEY 2400 Source Meter constant current source. The *EQE* values were calculated by the Lambertian distribution. Transient electroluminescence of the devices was measured using a Keysight 33622A function generator, Yokogawa DL9140 oscilloscope, HAMAMATSU G1760001 photomultiplier, and DHPCA-100 current amplifier.

Synthesis and Characterization

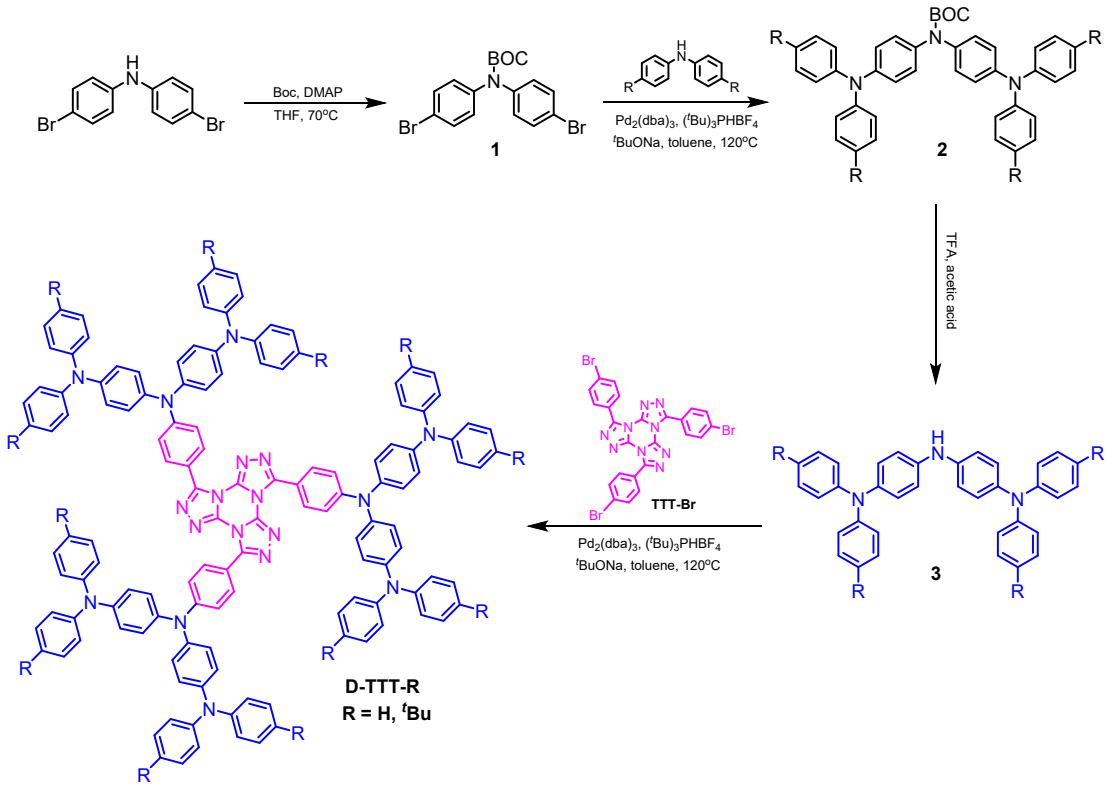

Scheme S1. Synthetic route of the compound D-TTT-R

Synthesis of 1

Bis(4-bromophenyl)amine (1 eq.), 4-(N,N-dimethylamino)pyridine (0.2 eq.), and di-tert-butyl decarbonate (1.5 eq.) were dissolved in dry THF (15 mL) under N_2. The yellow solution was heated to reflux for 3 h. After it was cooled to room temperature and the subsequent removal of the solvent on a rotary evaporator, the residue was purified by column chromatography to obtain the compound. solid (using petroleum ether/CH2Cl2 = 1:5 (v/v) as the eluent,514 mg, 80%). ^{1}H NMR (400 MHz, $CDCl_3$) δ 7.82 (s, 1H), 7.43 (d, *J* = 18.7 Hz, 4H), 7.12 (d, *J* = 8.5 Hz, 3H), 1.43 (s, 9H).

Synthesis of 3

Compound 2 (1eq.), compound (diphenylamine or 4,4'-di-tert-butyl diphenylamine 4eq), ^{t}BuONa (4eq.), Pd2(dba)3 (0.06eq.), and (HPtBu3)BF4 (0.12eq.) were dissolved in dry and deoxygenated toluene (30 mL) under nitrogen. The reaction mixture was heated to 120 °C for 19 h. Water (100 mL) was added to the cooled mixture, and the aqueous phase was extracted with dichloromethane (3 × 50 mL). The combined organic phases were dried over anhydrous $MgSO_4$, and subsequently the solvent was evaporated. The residue was purified by column chromatography to obtain the compound.

Boc-3TPA-H: White solid (using petroleum ether/CH_2Cl_2 = 1:2(v/v) as the eluent,(1.35 g, 55%). ^{1}H NMR (400 MHz, DMSO) δ 7.30 (s, 8H), 7.14 (s, 4H), 6.98 (d, *J* = 17.5 Hz, 16H), 1.38 (s, 9H).

Boc-3TPA-^{t}Bu: White solid (using petroleum ether/CH_2Cl_2 = 2:1 (v/v) as the eluent,5.5 g. 93%). ^{1}H NMR (500 MHz, $CDCl_3$) δ 7.23 (d, *J* = 8.7 Hz, 8H), 7.03 (dt, *J* = 16.0, 8.1 Hz, 16H), 1.46 (s, 9H), 1.30 (s, 36H).

Synthesis of 4

Compound 3 (1eq.) was dissolved in acetone (40 mL) under nitrogen. Trifluoroacetic acid (TFA, 5eq.) was added drop by drop, and the solution was stirred at room temperature

overnight. Then the reaction mixture was evaporated to dryness. The residue was purified by column chromatography to obtain the compound.

3TPA-H: White solid (using petroleum ether/CH_2Cl_2 = 2:1 (v/v) as the eluent,810 mg. 90%). ^{1}H NMR (400 MHz, DMSO) δ 7.24 (s, 11H), 6.97 (d, *J* = 8.2 Hz, 18H).

3TPA-^{t}Bu: White solid (using petroleum ether/CH2Cl2 = 7:1 (v/v) as the eluent,3.2 g, 67%). ^{1}H NMR (400 MHz, $CDCl_3$) δ 7.31 – 7.25 (m, 8H), 7.12 – 7.02 (m, 16H), 1.32 (s, 36H).

Synthesis of 5

Compound 1(1 eq.), Compound 4(3TPA-H or 3TPA-^{t}Bu 5 eq.), sodium tert-butoxide (4 eq.), $Pd_2(dba)_3$ (0.06 eq.), $(tBu)_3PHBF_4$ (0.12 eq.) and toluene (40 mL) were added to a 200 mL round-bottom flask. The mixture was stirred at 120^{o}C for 24 h under a nitrogen atmosphere. After cooling to room temperature, the mixture was poured into water and extracted with CH_2Cl_2 (3 × 50 mL). The combined organic layers were washed with water, dried over anhydrous $MgSO_4$ and evaporated to dryness. The residue was purified by column chromatography to obtain the compound.

TTT-3TPA-H: White solid (using petroleum ether/CH_2Cl_2 = 2:1(v/v) as the eluent, 186 mg, 27.6%).^{1}H NMR (400 MHz, $CDCl_3$) δ(ppm): 8.05 (s, 6H), 7.28 (s, 18H), 7.09 (d, *J* = 20.6 Hz, 72H). TOF-MS(ESI) m/z calcd for $C_{132}H_{96}N_{18}$: 1932.81 $[M]^+$; found: 1930.50.

TTT-3TPA-^{t}Bu: White solid (using petroleum ether/CH_2Cl_2 = 2:1 (v/v) as the eluent, 96 mg, 12.3%).^{1}H NMR (400 MHz, $CDCl_3$) δ(ppm): 8.07 (d, *J* = 8.8 Hz, 6H), 7.34 – 7.30 (m, 26H), 7.16 – 7.06 (m, 52H), 1.36 (s, 108H). TOF-MS(ESI) m/z calcd for $C_{180}H_{192}N_{18}$: 2605.56 $[M]^+$; found:2604.70. HPLC: 97.6%.

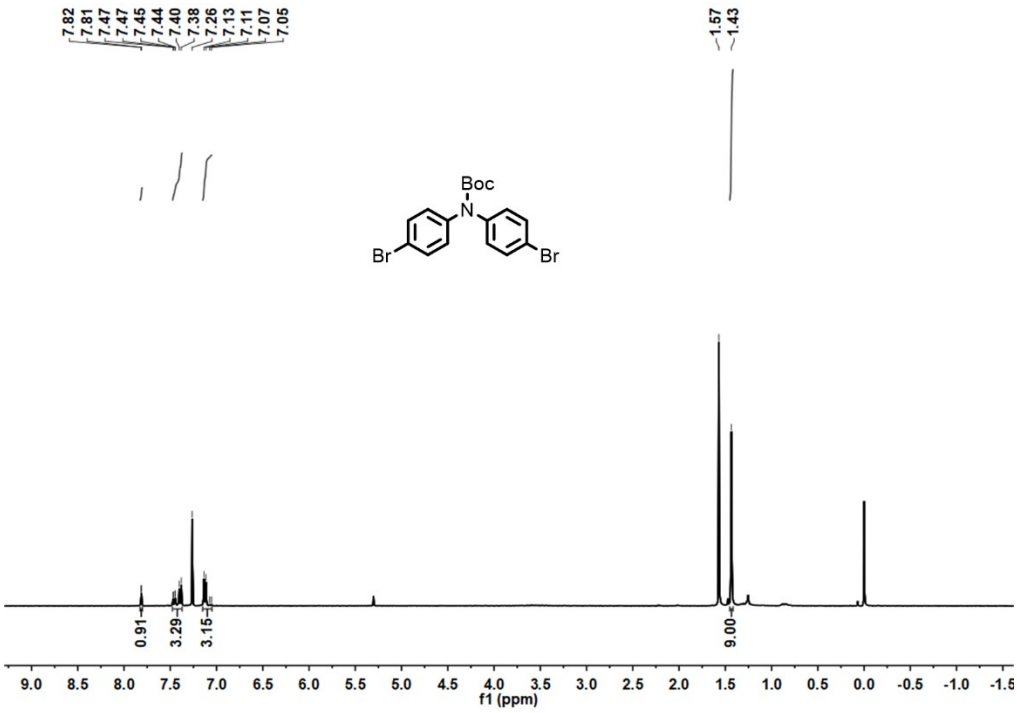

Figure S1. ^{1}H NMR spectrum of 1 in $CDCl_3$ at room temperature

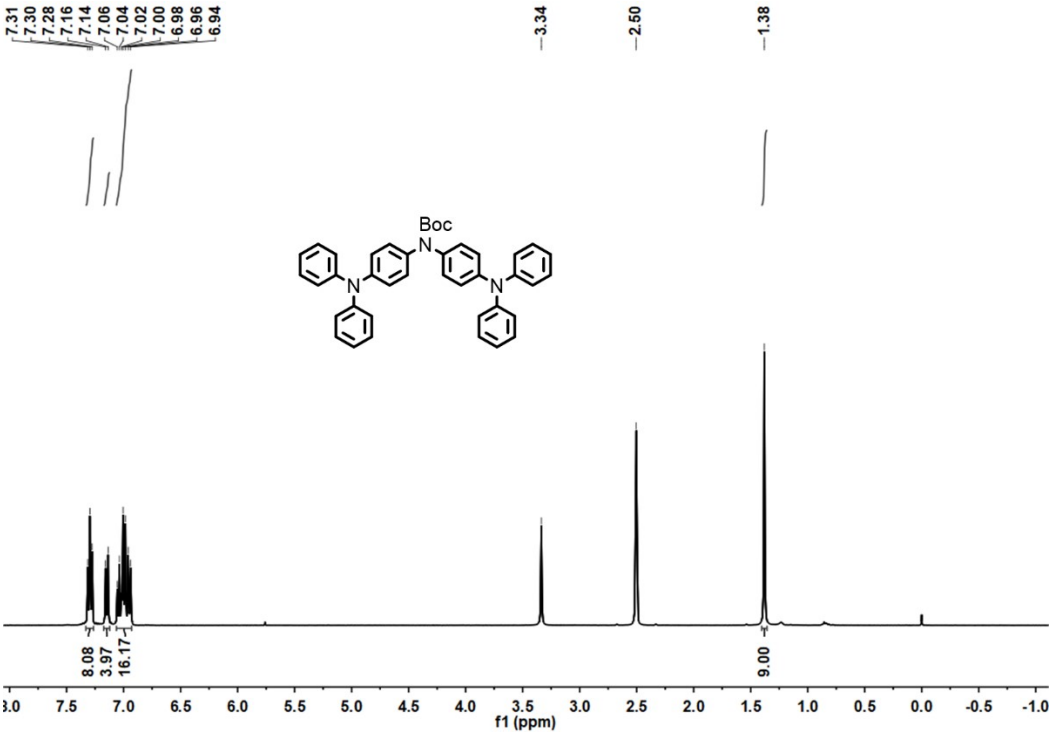

Figure S2. ^{1}H NMR spectrum of Boc-3TPA-H in DMSO at room temperature

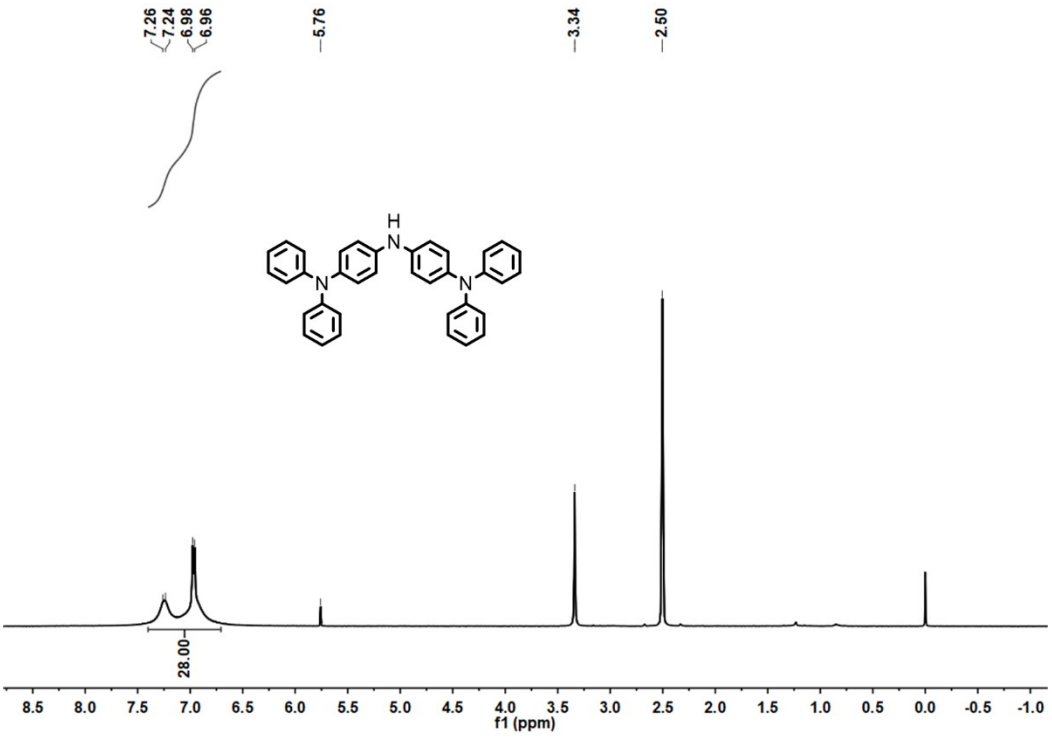

Figure S3. ^{1}H NMR spectrum of Boc-3TPA -^{t}Bu in $CDCl_3$ at room temperature

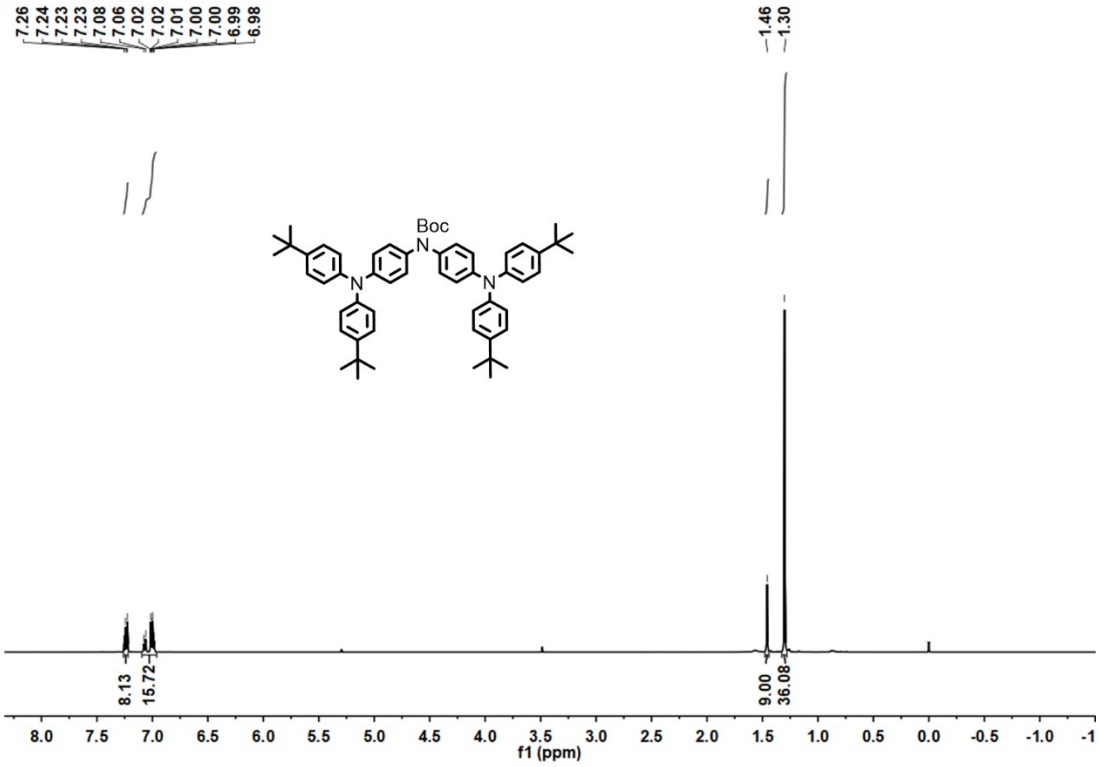

Figure S4. ^{1}H NMR spectrum of 3TPA-H in DMSO at room temperature

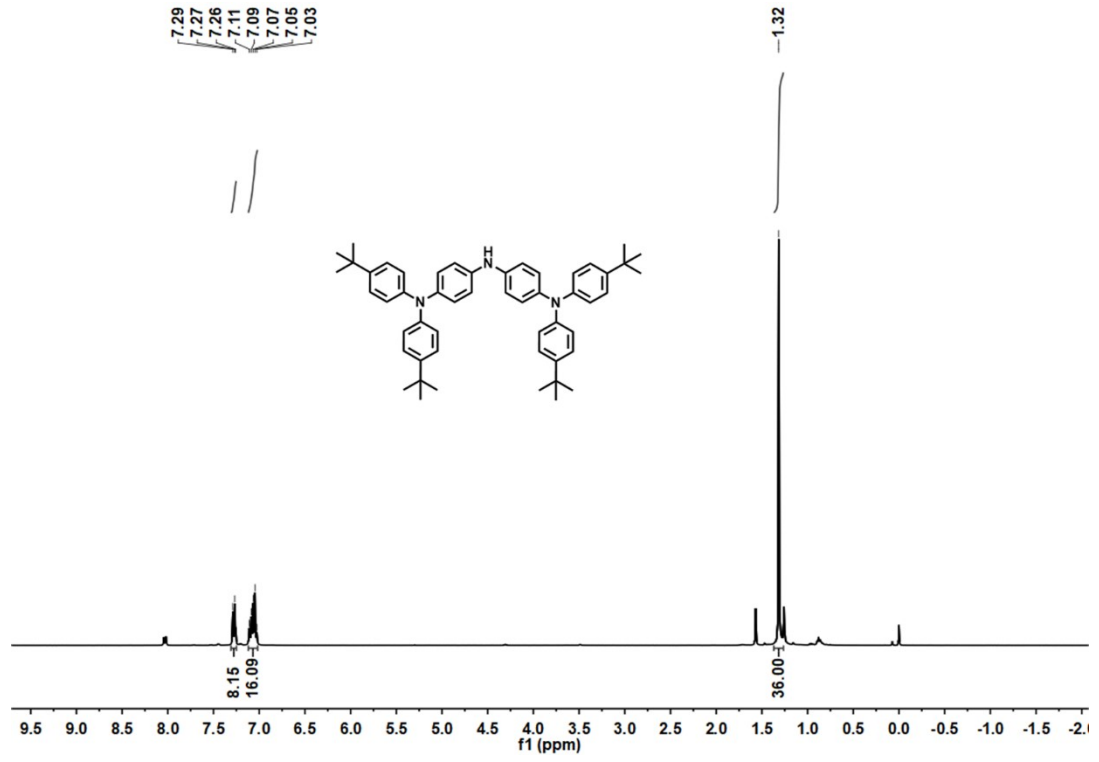

Figure S5. ^{1}H NMR spectrum of 3TPA-^{t}Bu in $CDCl_3$ at room temperature

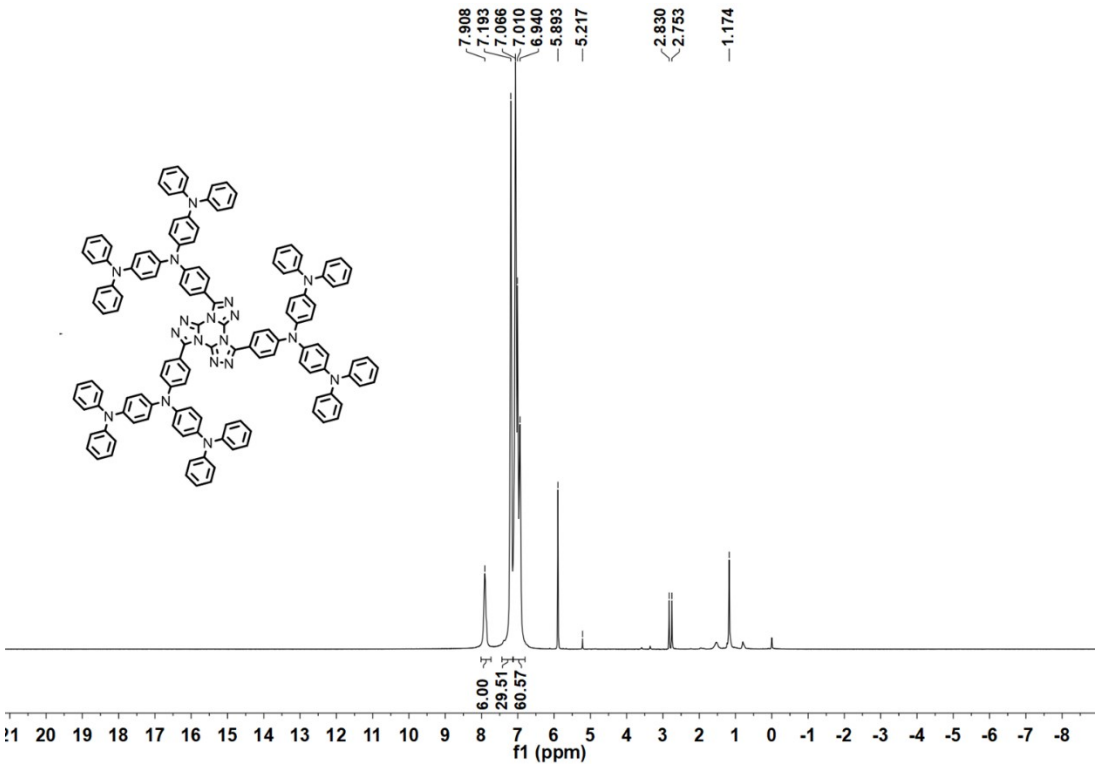

Figure S6. ^{1}H NMR spectrum of D-TTT-H in $CDCl_3$ at room temperature

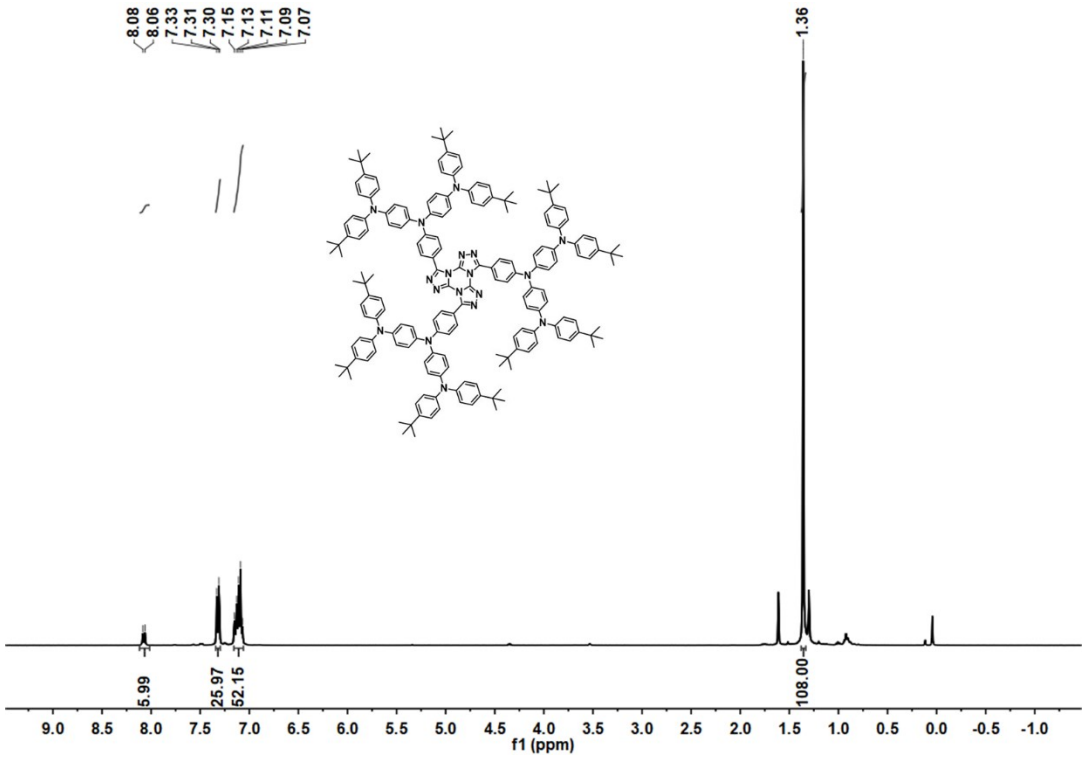

Figure S7. ^{1}H NMR spectrum of D-TTT-^{t}Bu in $CDCl_3$ at room temperature

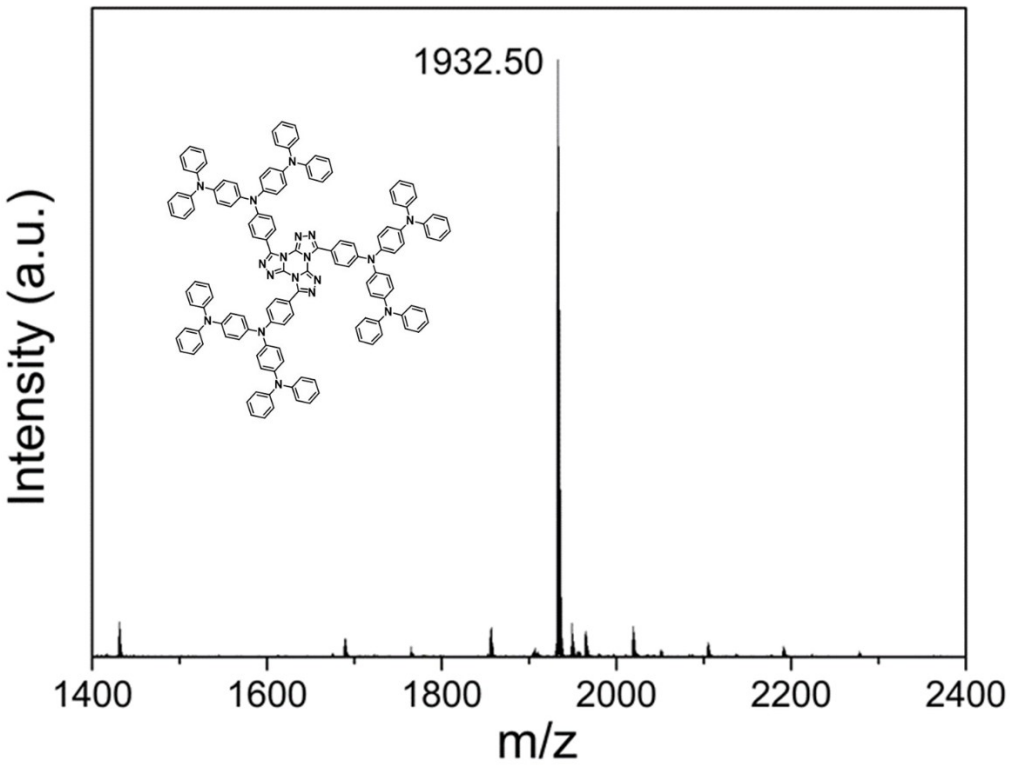

Figure S8.TOF-MS spectrum of D-TTT-H in CH_2Cl_2 at room temperature

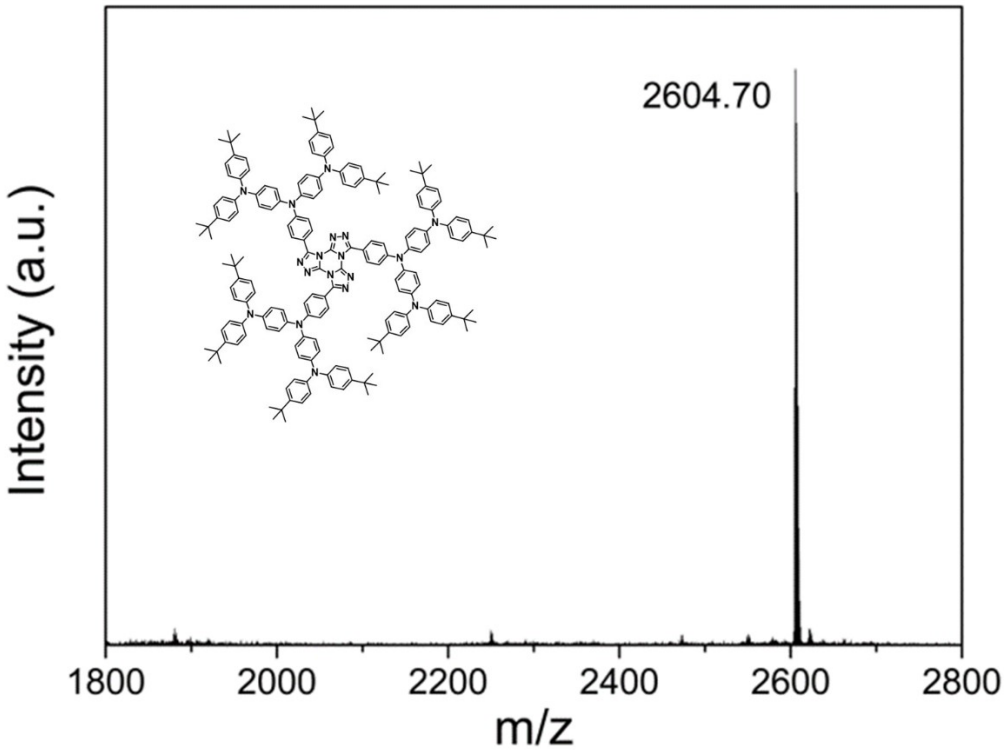

Figure S9.TOF-MS spectrum of D-TTT-^{t}Bu in CH_2Cl_2 at room temperature

Photophysical Property and EL performance

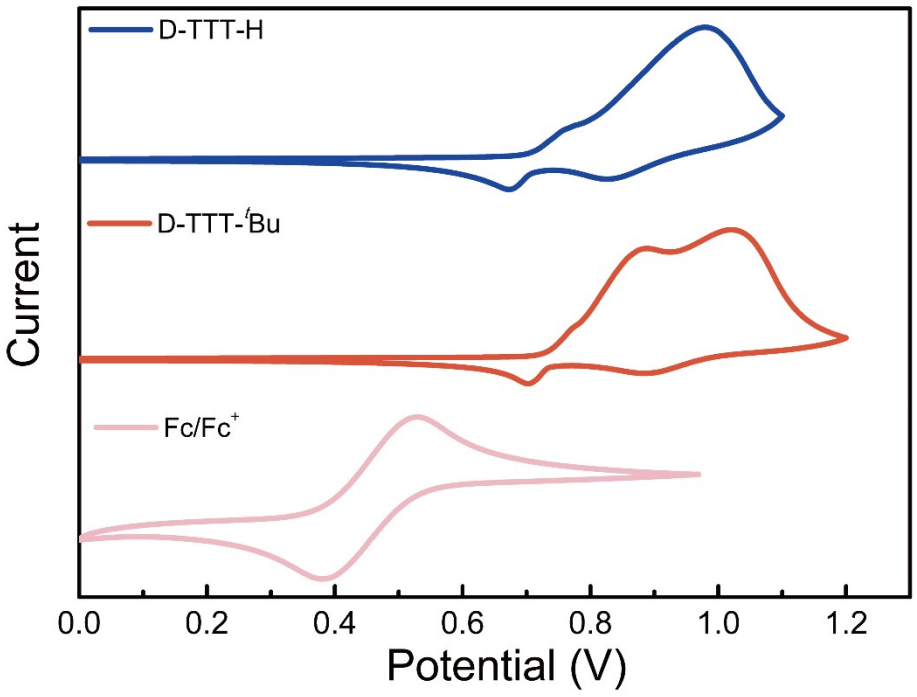

Figure S11. CV curves of the dendrimers in $CHCl_3$ solution (the x axis vervus Ag/Ag^+).

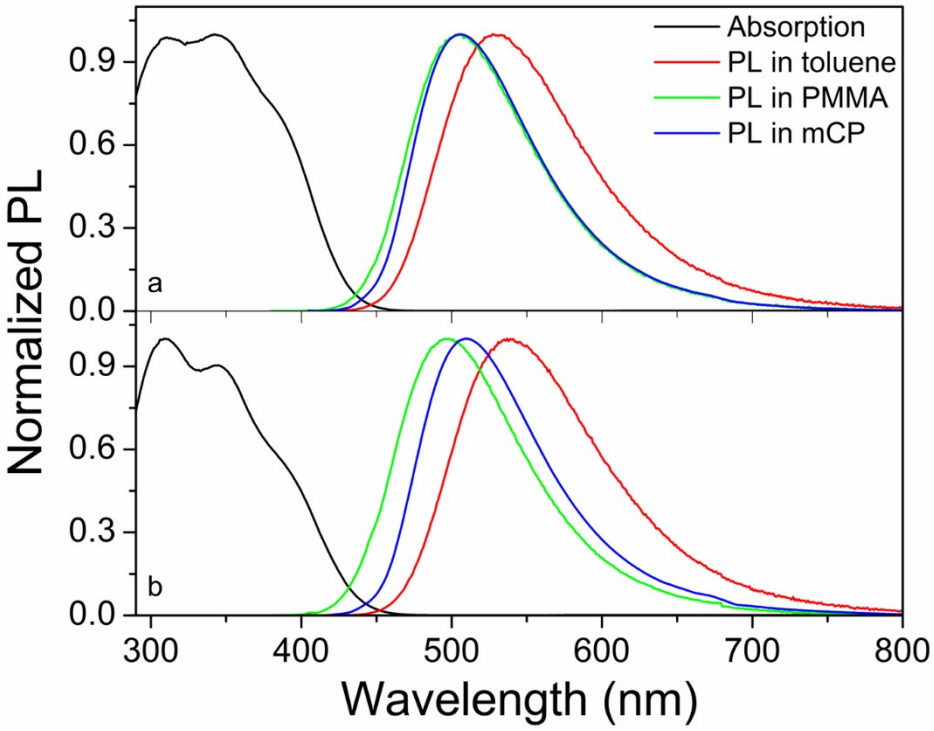

Figure S12. UV-vis and PL spectra of the compounds in toluene solution (10^{-5} M) at room temperature (a: D-TTT-H; b: D-TTT-^{t}Bu; excitation wavelength is 380 nm).

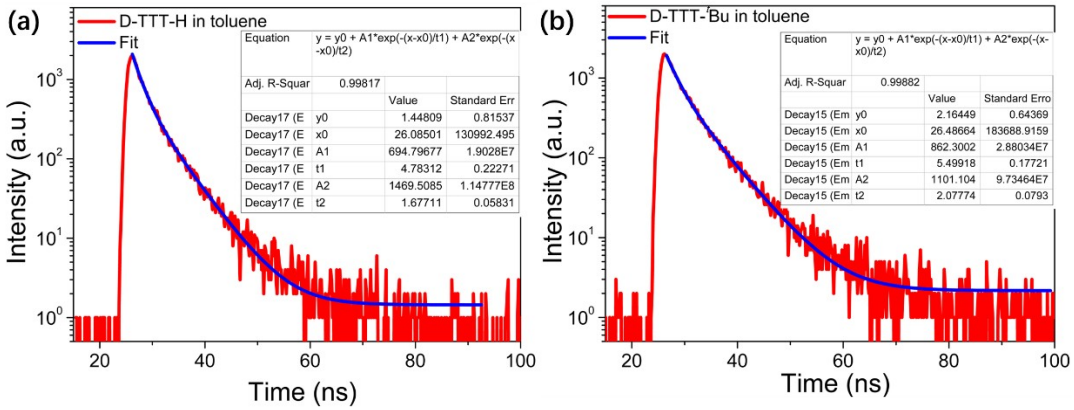

Figure S13. The fitting linear of D-TTT-H (a) and D-TTT-^{t}Bu (b) in toluene.

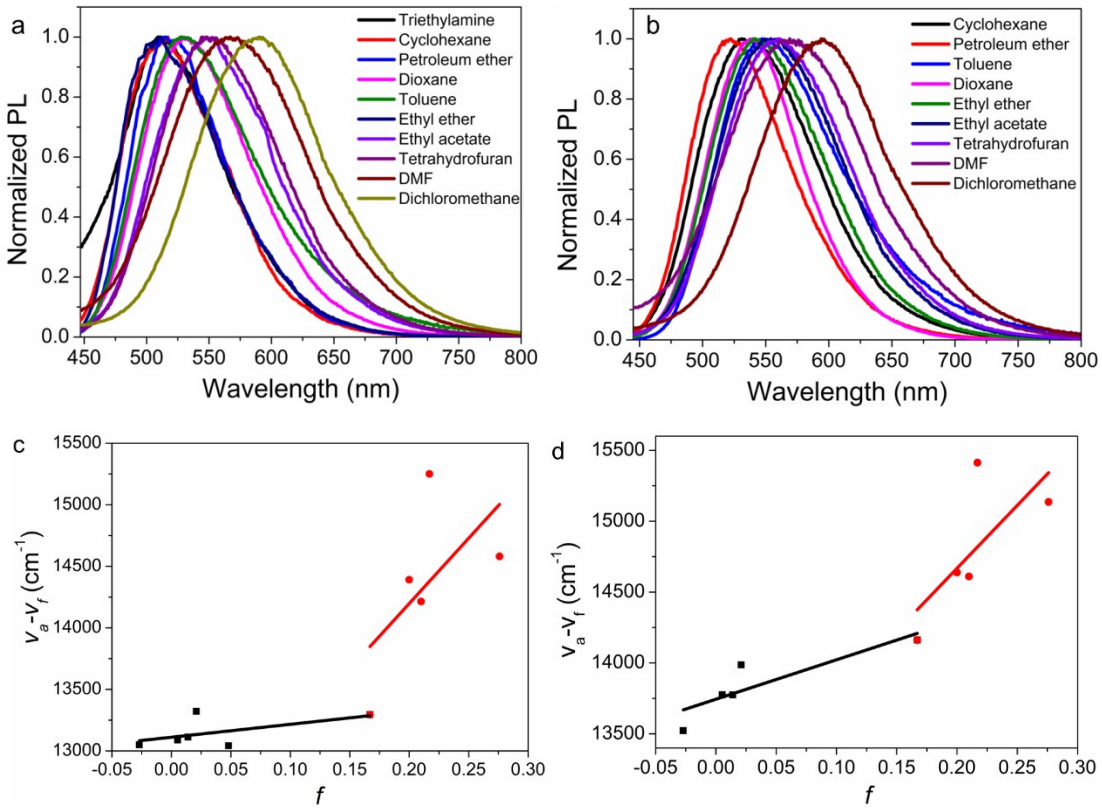

Figure S14. Solvatochromic PL spectra of D-TTT-H (a) and D-TTT-^{t}Bu (b) and Lippert–Mataga plots of the Stokes shift of D-TTT-H (c) and D-TTT-^{t}Bu (d) against the solvent polarity parameters.

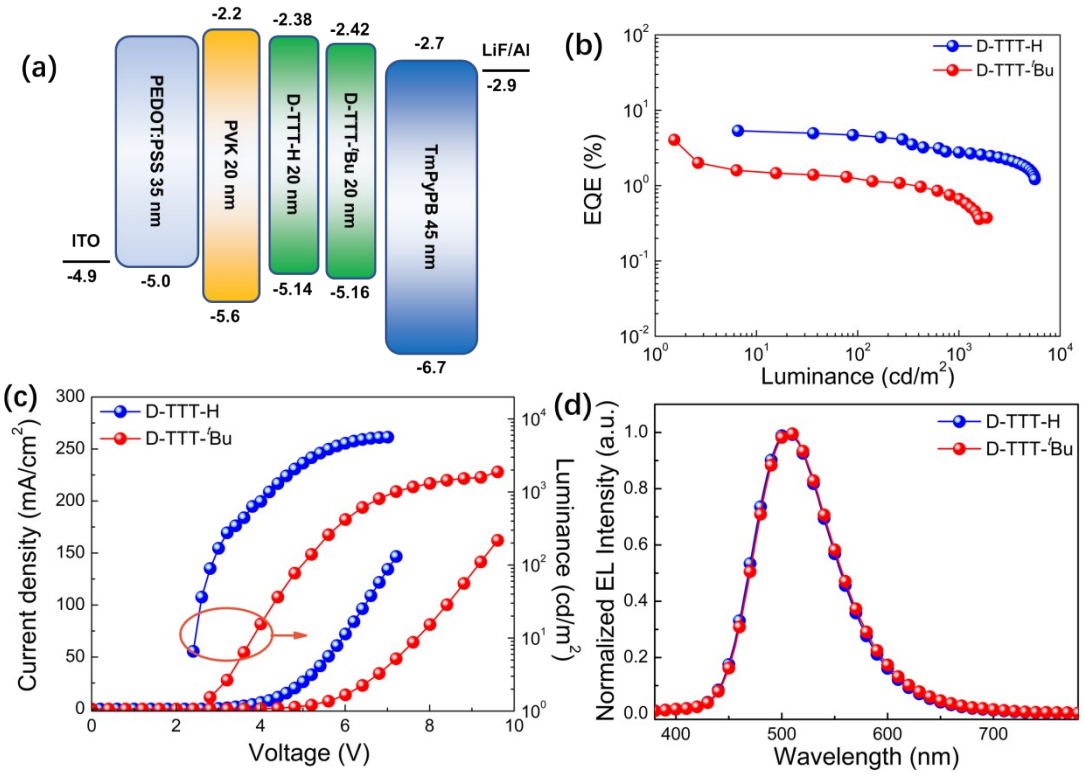

Figure S15. a) Device structure of non-doped devices (D1 and D2); b) *EQE*-Luminance curves; c) Current density-Voltage-Luminance curves; d) EL spectra of the devices.

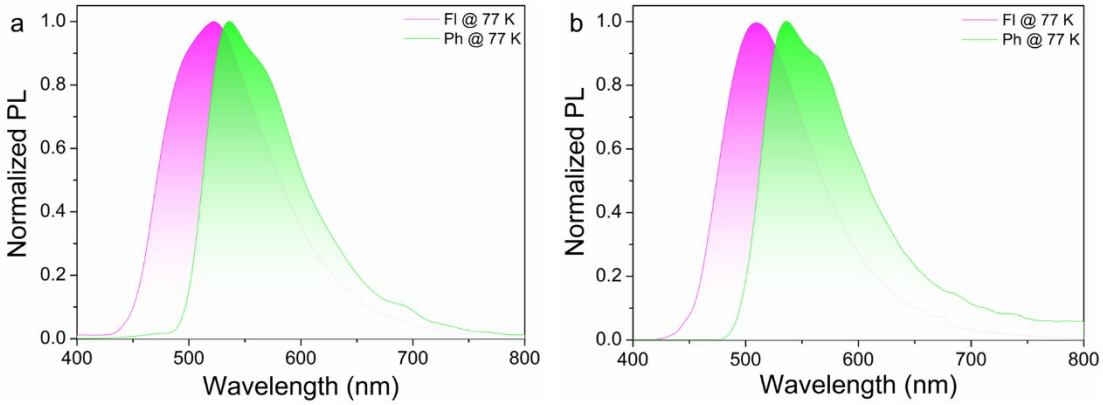

Figure S16. Low temperature of fluorescence and phosphorescence spectra (a: D-TTT-H and b: D-TTT-^{t}Bu) of 20 wt% emitter doped in mCP film.

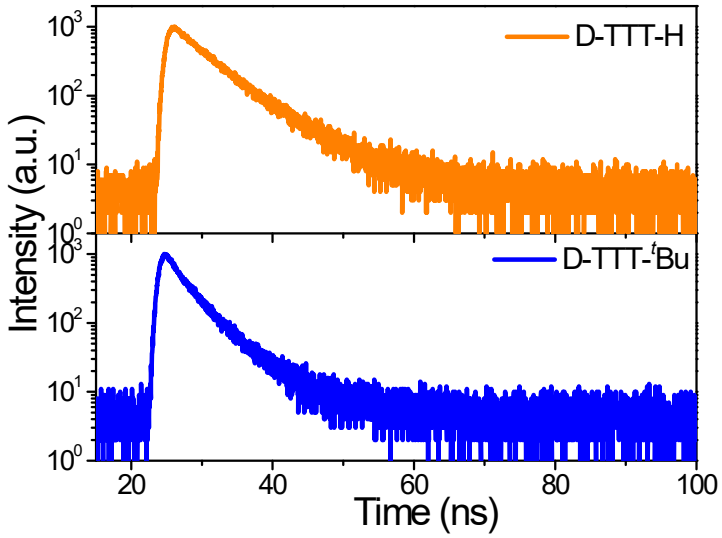

Figure S17. Transient PL prompt decay of the doped-mCP film (ex: 450nm).

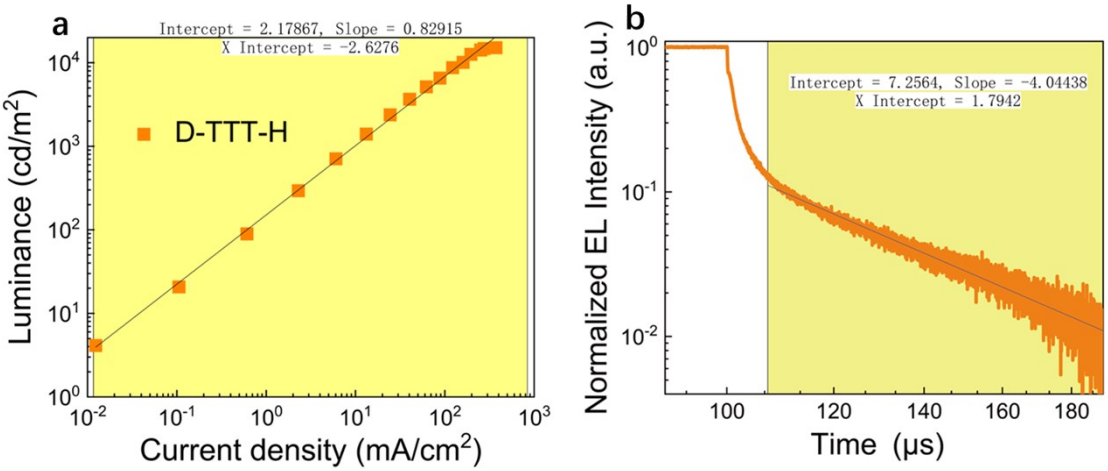

Figure S18. a) The fitting result of luminance-current density curve; b) the fitting result of transient electroluminescence decay curve at 50 cd m^{-2}.

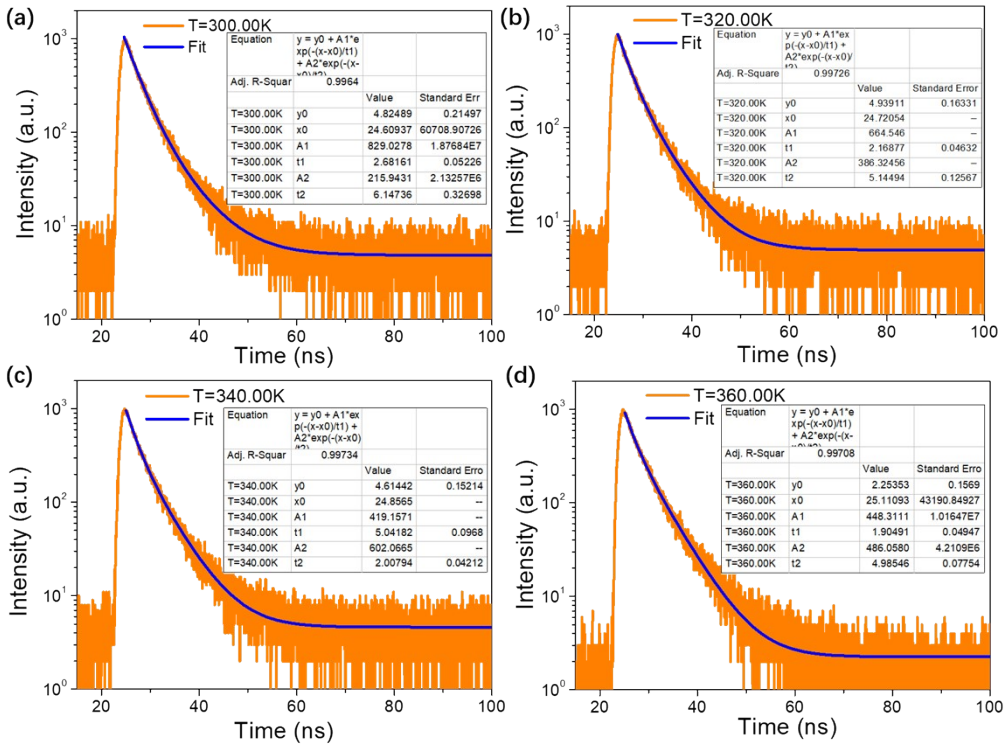

Figure S19. The fitting linear of the doped film (mCP: 20 wt% D-TTT-H) at different temperature

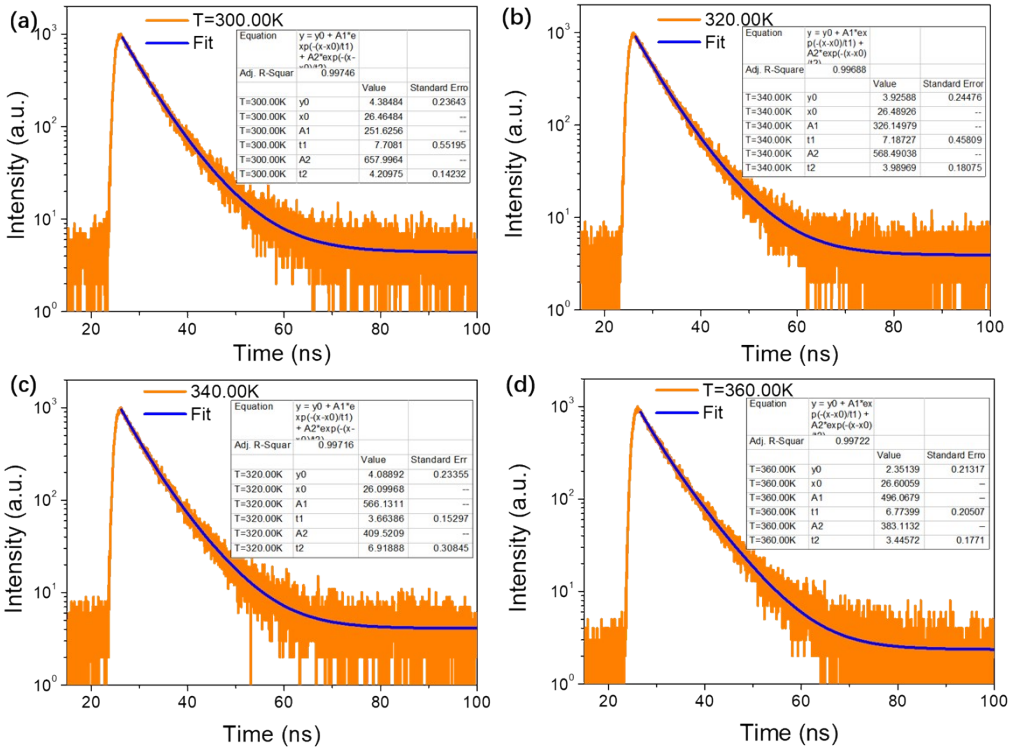

Figure S20. The fitting linear of the doped film (mCP: 20 wt% D-TTT-*t*Bu) at different temperature

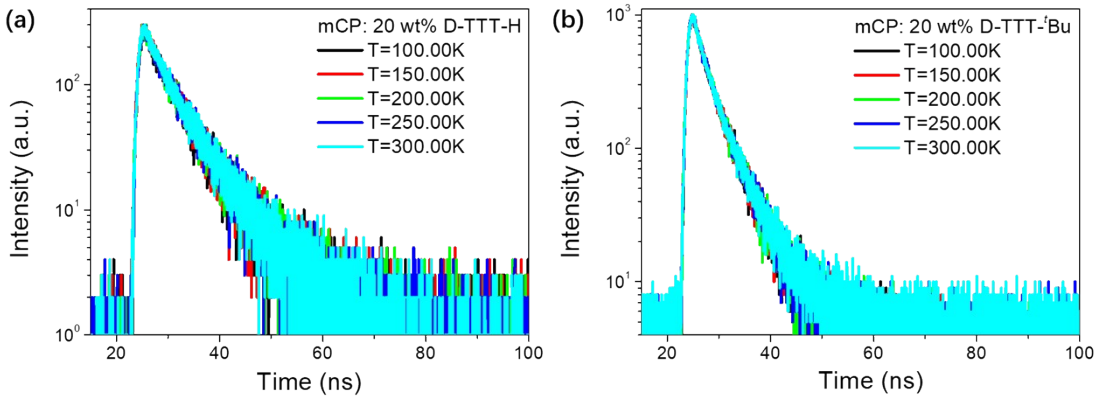

Figure S21. The transient PL prompt decay curves the doped film at different temperature

MEL's Arguments Details

1. Exclusion of TTA process

According to Merrifield theory, under no external magnetic field condition, in a typical TTA-based OLED, a generated TT-pair exhibits 1/9 of singlet, 3/9 of triplet, and 5/9 of quintet characteristics. Therefore, in the low magnetic field region (<50 mT), where the internal Zeeman splitting intensity due to hyperfine interactions and spin–orbit coupling is similar to the external Zeeman splitting intensity, the singlet character of the TT-pair can increase up to 3/9. These additional 'bright' singlet states can contribute as light, increasing MEL intensity. In contrast, in the high magnetic field region (>50 mT), the transition rate of TT-pairs into singlets decreases.[1, 2] Consequently, when a magnetic field is applied to a TTA-based OLED, the fingerprint of the MEL signal intensity increases in the low magnetic field region, followed by a decreasing signature in the high magnetic field region. (See the MEL signal at 10 V in **Figure S22a** for example).[3] These MEL characteristics are more pronounced in the high current density (or voltage) region since the population density of triplets is higher in the high current density (or voltage) region as shown in **Figure S22a**.

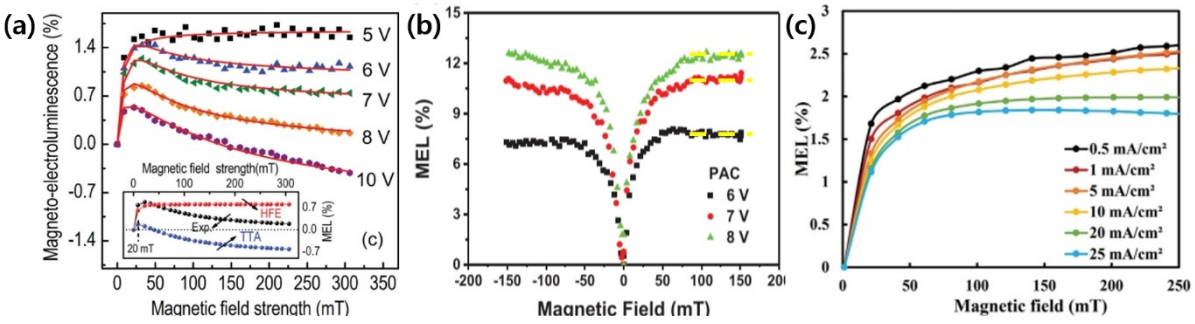

Figure 22. (a) Typical MEL data of TTA material, (b) MEL data of HLCT material, (c) MEL data of HLCT and TTA material

In the case of non-doped OLEDs with pure HLCT materials as shown in **Figure S22b**, the MEL signals rise with increasing voltage.[4] Additionally, the MEL intensity remains unvaried in the high magnetic field region (>50 mT), as indicated by the yellow dashed lines.

For materials exhibiting dual characteristics of HLCT and TTA, as demonstrated in the high field in **Figure S22c**, two distinctive features emerge compared to TTA-only or HLCT-

only devices.[5] Specifically, the MEL intensity and slope in the high magnetic field region decrease with increasing applied voltage, reflecting characteristics of both TTA and HLCT simultaneously.

The MEL signals from the non-doped device with D-TTT-H exhibit constant intensities in the high field region, a distinctive fingerprint of HLCT characteristics. Furthermore, the slope in the high magnetic field region remains unchanged with variations in applied voltage. Thus, the possibility of TTA in the D-TTT-H device can be ruled out. Nevertheless, the MEL intensity itself decreases with increasing applied voltage, suggesting the coexistence of unknown exciton dynamics alongside the HLCT mechanism.

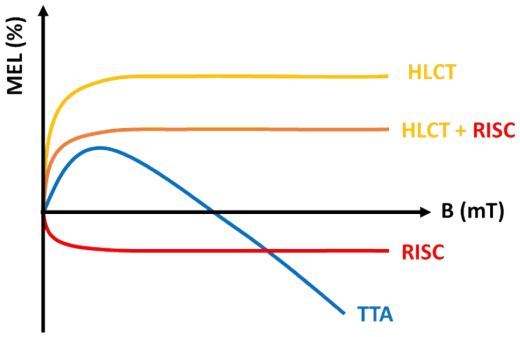

Figure S23. The schematic MEL characteristics of different exciton dynamics

2. Presence of TADF process

As shown in **Figure S23**, the TADF (RISC) process in polaron-pair (PP) states contributes to MEL as an inverted Lorentz line, because the Zeeman splitting of PP with triplet characteristics leads to a suppression of spin mixing. Consequently, there is a reduction in singlet density, which, in turn, contributes to emission. However, the external magnetic field has a limited impact on triplet exciton states. Thus, in the presence of the RISC mechanism, the MEL intensity is affected only in the low magnetic field region (<50 mT), remaining constant in the high magnetic field region, as illustrated by the red line in **Figure S23**.

When all excitonic processes occur simultaneously and competitively in the emissive layer (EML) (refer to Figure 1 in the manuscript), both processes manifest in the MEL signals, as

depicted by the orange line in **Figure S23**. This representation corresponds to the MEL characteristics in **Figure 3e** in the manuscript. The slight variations observed in the MEL curves in **Figure 3f** of the doped device may be attributed to mixed exciton dynamics originating from the mCP host.

Computational Details

The amorphous aggregates were obtained by molecular dynamic (MD) simulations in a cubic box of 2.9 nm × 2.9 nm × 2.9 nm with the general amber force field (GAFF). The initial structures were first energy minimized with the steepest descent algorithm and then relaxed for 50 ps in the NVT ensemble. Subsequently, 8 ns NPT simulations were performed. The temperature was 298.15 K and the pressure was 1 bar. Periodic boundary conditions were applied in all three dimensions to minimize the edge effects in a finite system. Here, the time step was 2 fs and the configurations were stored at a time interval 1 ps for data analysis. Conformations were extracted from MD trajectories within the final 3 ns to calculate the radial distribution function of three torsion angle (θ_1, θ_2 and θ_3) by VMD.[6] All MD calculations were done by using GROMACS-2018.4 package.[7]

The equilibrium configuration of the ground state (S_0) in gas was performed at the B3LYP/6-31G(d) level in Gaussian 09 package.[8] For the solid-state geometry, we extracted the configuration from MD calculations with the representative twisted angles (θ_1=31°, θ_2=43° and θ_3=41°). Subsequently, we employed TD-B3LYP/6-31G(d) within the Orca package[9] to assess their excited-state electronic structures, including excitation energies, natural transition orbitals and spin-orbit coupling matrix elements. Additionally, the overlap integral of HOMO and LUMO (S_{HL}) was calculated by using Multiwfn.[10]

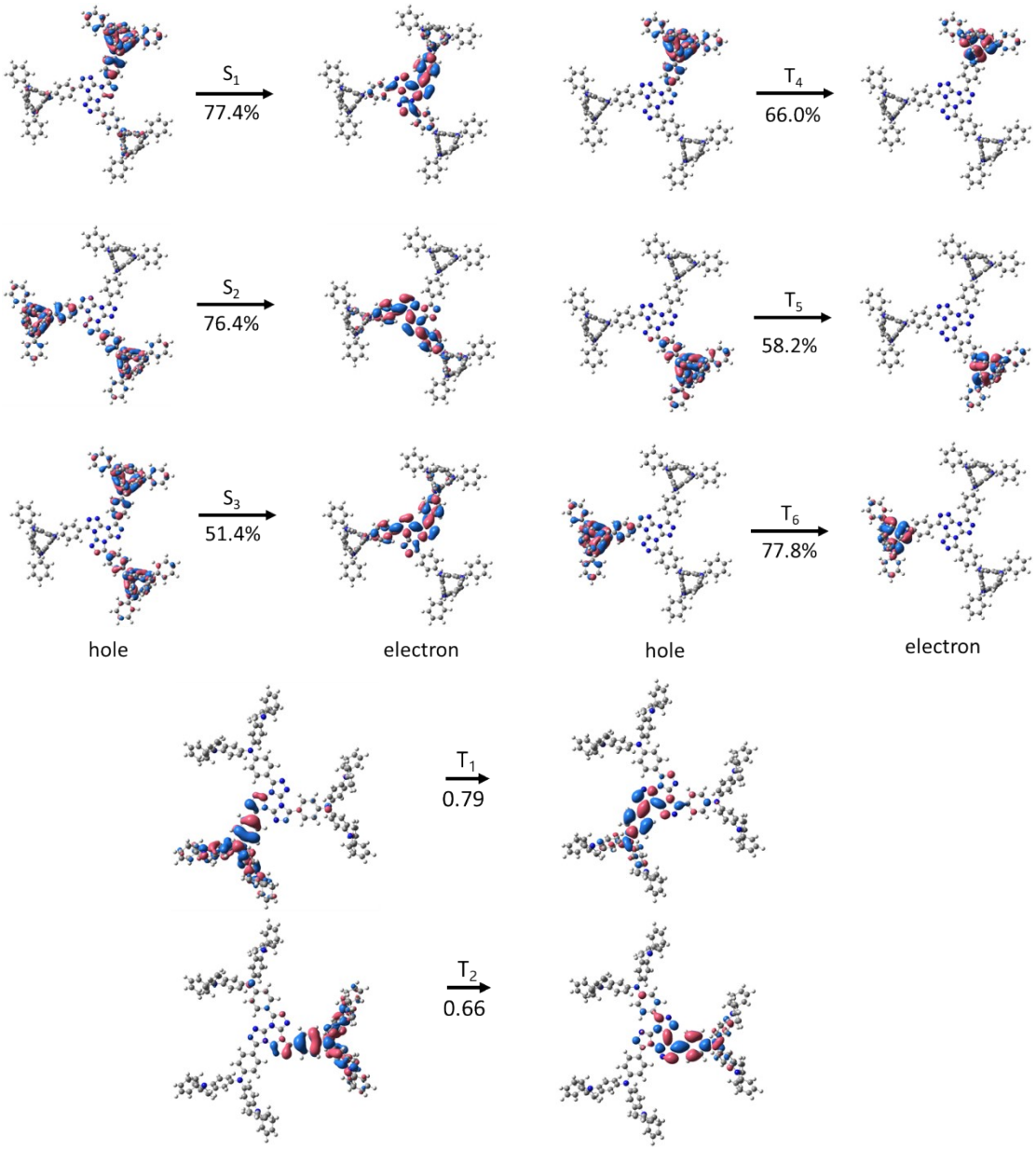

Figure S24. The natural transition orbitals (NTOs) of both singlet and triplet excited states for D-TTT-H ($S_1 \rightarrow S_0$, $S_2 \rightarrow S_0$, $S_3 \rightarrow S_0$, $T_1 \rightarrow S_0$, $T_2 \rightarrow S_0$, $T_4 \rightarrow S_0$, $T_5 \rightarrow S_0$, and $T_6 \rightarrow S_0$).

The Out-Coupling Efficiencies Related Supplements

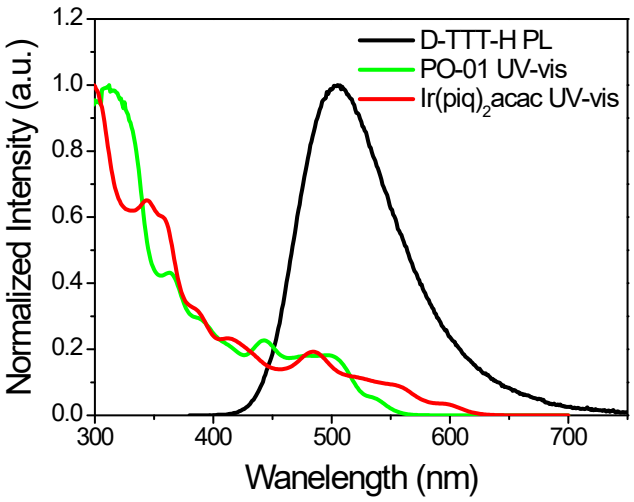

Figure S25. The overlap between D-TTT-H PL and PO-01, $Ir(piq)_2acac$ UV-vis

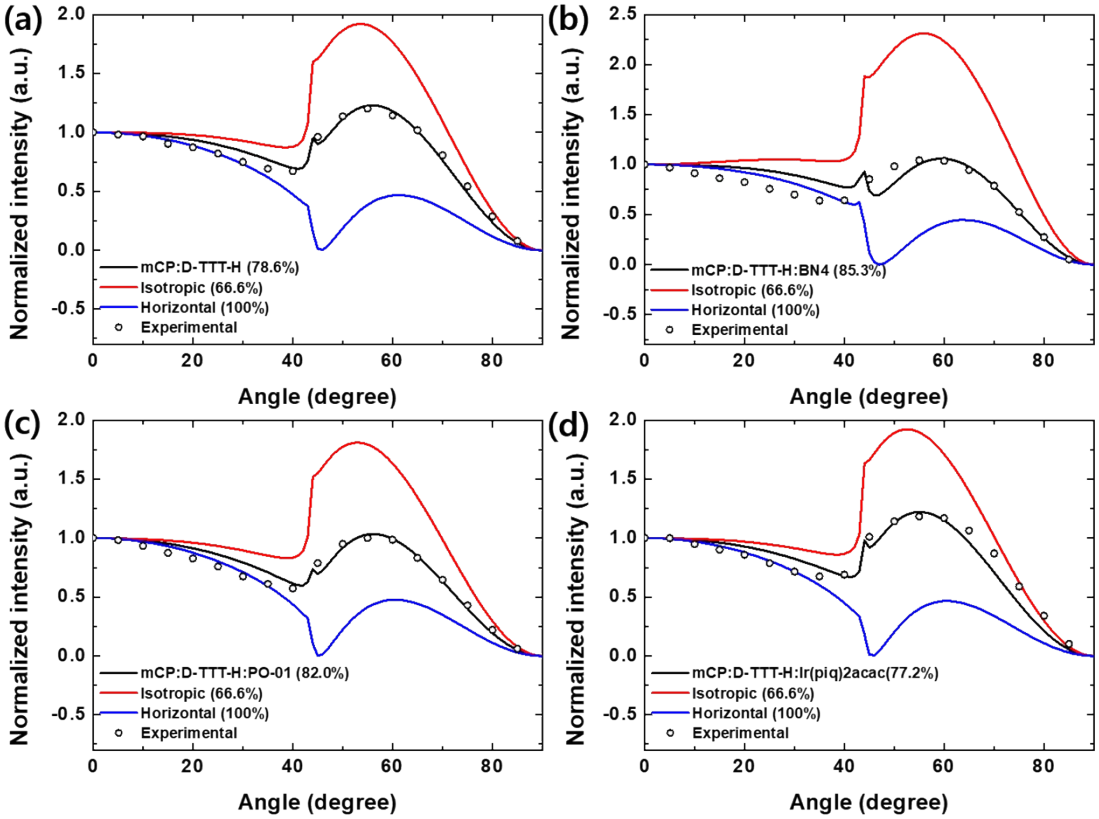

Figure S26. Measured horizontal transition dipole moment ratio of the doped film of (a) mCP : D-TTT-H, (b) mCP : D-TTT-H : BN4, (c) mCP : D-TTT-H : PO-01 and (d)mCP : D-TTT-H : $Ir(piq)_2acac$.

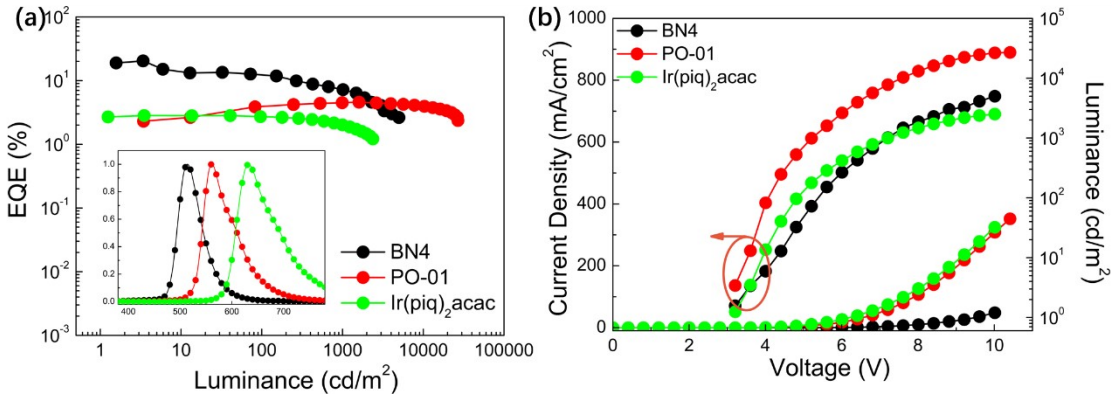

Figure S27. EL performance for the non-sensitizer devices: a) EQE-Lumminance (inset: EL spectra) and b) Current density-Voltage-Luminance of the non-sensitized devices (mCP: 5 wt% dopant)

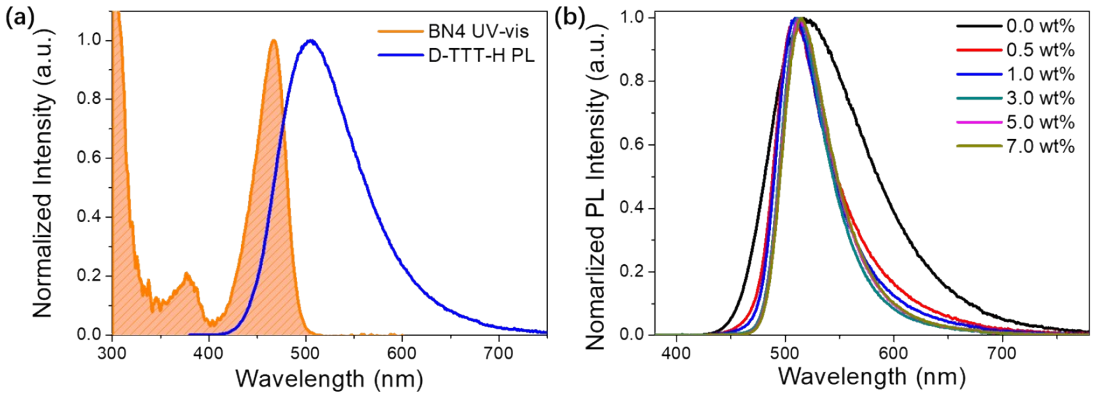

Figure S28. a) Spectral overlap between the sensitizer (D-TTT-H) and dopant (BN4); b) PL spectra of the doped films (mCP: 30 wt% D-TTT-H: x wt% BN4) at different concentration.

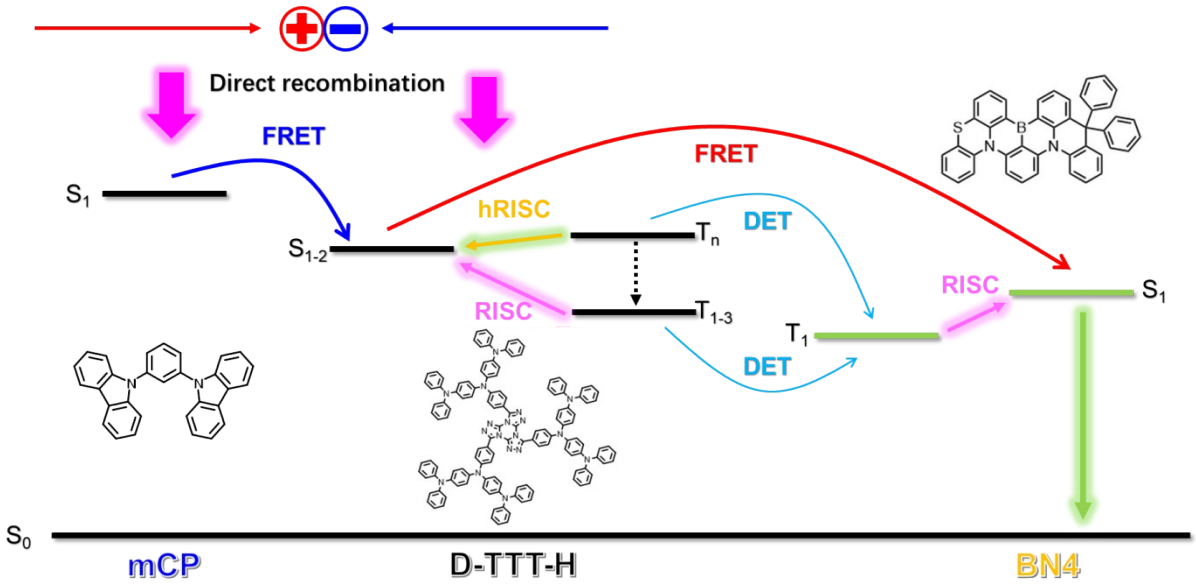

Figure S29. Schematic diagram for the processes of the sensitized OLED. FRET: Förster resonance energy transfer; DET: Dexter energy transfer.

TrEL Data Supplement

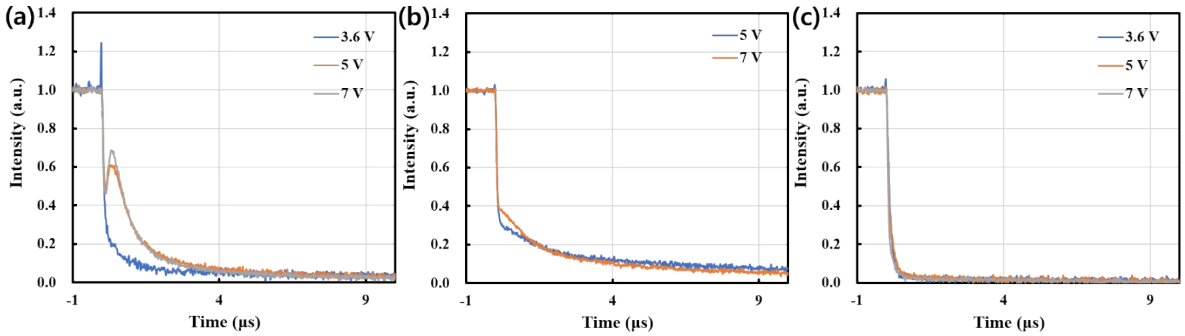

Figure S30. Transient EL decay curves of (a) mCP:20 wt% D-TTT-H, (b) mCP:20 wt% D-TTT-^{t}Bu and (c) D-TTT-H

Table S1. Photophysical date of the dendrimers (20 wt%) doped in mCP films

	Hot exciton process		TADF process	
	D-TTT-H	D-TTT-^{t}Bu	D-TTT-H	D-TTT-^{t}Bu
ϕ_{PL} [%]	63.67	43.05	65.16	46.23
τ_{prompt} [ns]	4.21	2.68	4.32	3.70
$\tau_{delayed}$ [ns/μs]	7.71/-	6.15/-	-/1.32	-/8.67
ϕ_{prompt} [%]	37.45	26.94	63.67	43.05
$\phi_{delayed}$ [%]	26.22	16.11	1.49	3.18
$^a k_{ISC}$ [s^{-1}]	0.98×10^8	1.40×10^8	8.41×10^7	1.54×10^7
$^b k_{RISC}$ [s^{-1}]	2.21×10^8	2.60×10^8	4.88×10^4	1.50×10^4

a: hot exciton process; b: TADF process.

Table S2. Photophysical date for the hRISC process in solution

	D-TTT-H in toluene	D-TTT-^{t}Bu in toluene	mCP: 20 wt% D-TTT-H	mCP: 20 wt% D-TTT-^{t}Bu
ϕ_{PL} [%]	81.24	75.50	63.67	43.05
τ_{prompt} [ns]	1.68	2.08	4.21	2.68
$\tau_{delayed}$ [ns]	4.78	5.50	7.71	6.15
ϕ_{prompt} [%]	34.73	24.53	37.45	26.94
$\phi_{delayed}$ [%]	46.51	50.97	26.22	16.11
K_{hISC} [s^{-1}]	3.41×10^8	3.25×10^8	0.98×10^8	1.40×10^8
K_{hRISC} [s^{-1}]	4.89×10^8	5.60×10^8	2.21×10^8	2.60×10^8

Table S3. EL performance of D-TTT-H and D-TTT-^{t}Bu based devices with different dopant concentration

Guest	Dopant /wt %	V_{ON} /V	L_{max} /cd m^{-2}	CE_{max} /cd A^{-1}	PE_{max} /cd A^{-1}	EQE_{max} /%	$Peak_{max}$ /nm	CIE
D-TTT-H	1	4.4	1617	6.01	4.27	2.65	486	(0.17,0.32)
	5	4.0	3607	7.62	5.43	3.04	492	(0.19,0.38)
	10	3.6	6096	27.61	24.07	9.84	504	(0.23,0.47)
	20	2.8	15090	33.39	37.37	11.96	504	(0.21,0.45)
	30	2.8	15780	18.59	20.82	6.58	504	(0.22,0.46)
D-TTT-^{t}Bu	1	5.6	1934	7.68	3.54	3.51	490	(0.18,0.34)
	5	4.4	2406	5.24	3.43	1.82	498	(0.20,0.40)
	10	4.0	3727	24.10	18.90	8.52	506	(0.24,0.48)
	20	3.2	8319	29.76	29.14	9.90	506	(0.23,0.49)
	30	3.2	7484	8.47	6.03	2.89	506	(0.23,0.49)

Table S4. EL performance of sensitized devices

	V_{ON} /V	L_{max} /cd m^{-2}	$CE_{max/100/1000}$ /cd A^{-1}	$EQE_{max/100/1000}$ /%	PE_{max} /lm W^{-1}	$Peak_{max}$ /nm	CIE
S1	2.8	4473	88.16/52.01/33.16	30.88/16.77/9.67	86.35	514	(0.21, 0.64)
S2	2.8	40090	78.50/75.75/54.59	24.08/23.31/16.65	76.93	560	(0.46, 0.52)
S3	2.8	2754	9.00/6.57/3.90	14.33/9.02/4.64	10.85	626	(0.66, 0.33)

Table S5. EL performance of non-sensitized devices

Guest	V_{ON} /V	L_{max} /cd m^{-2}	CE_{max} /cd A^{-1}	EQE_{max} /%	PE_{max} /cd A^{-1}	λ_{EL} /nm	CIE
BN4	3.2	4112	58.34	20.37	52.23	514	(0.21, 0.64)
PO-01	3.2	26910	14.98	4.57	9.98	562	(0.48, 0.51)
Ir(piq)$_2$acac	3.2	2507	1.71	2.82	1.41	632	(0.67, 0.32)

Table S6. Parameters for PLQY (in N_2) and the orientation factor (Θ)

Material	ϕ_{PL} %	Θ %
mCP: D-TTT-H	100	78.6
mCP: D-TTT-H: BN4	97.1	85.3
mCP: D-TTT-H: PO-01	87.8	82.0
mCP: D-TTT-H: Ir(piq)$_2$acac	65.4	77.2

Table S7. Parameters for Förster energy transfer process

Dopant concentration /wt%	R_0 /nm	R_{hg} /nm	k_{FRET} /10^7 S^{-1}	Φ_{ET} /%	Φ_{PL} /%
0.5	4.64	4.60	0.97	51.35	75.69
1	4.64	3.65	1.04	80.85	88.42
3	4.64	2.53	1.07	97.43	95.66
5	4.64	2.14	1.19	99.06	99.83
7	4.64	1.91	1.48	99.52	97.59

References

1. R. E. Merrifield, *Pure Appl. Chem.*, **1971**, 27, 481-498.
2. R. E. Merrifield, *J. Chem. Phys.*, **2003**, 48, 4318-4319.
3. P. Chen, Z. Xiong, Q. Peng, J. Bai, S. Zhang and F. Li, *Adv. Opt. Mater.*, **2014**, 2, 142-148.
4. Y. Xu, X. Liang, X. Zhou, P. Yuan, J. Zhou, C. Wang, B. Li, D. Hu, X. Qiao, X. Jiang, L. Liu, S.-J. Su, D. Ma and Y. Ma, *Adv. Mater*., **2019**, 31, 1807388.
5. H. Lee, V. V. Patil, J. Lim, B. K. Min, Y. M. Rhee, Y. K. Kim, T. Kim and J. Y. Lee, *Adv. Opt. Mater.*, **2022**, 10, 2200256.
6. W. Humphrey, A. Dalke, K. Schulten, *J. Mol. Graph. Model.* **1996**, 14, 33.
7. F. Neese, *Wires Comput. Mol. Sci.* **2018**, 8, e1327.
8. Frisch, M.J., Trucks, G.W., Schlegel, H.B., Scuseria, G.E., Robb, M.A., Cheeseman, J.R., et al. (2013) Gaussian 09, Revision D.01. Gaussian Inc., Wallingford CT.
9. M. J. Abraham, T. Murtola, R. Schulz, S. Páll, J. C. Smith, B. Hess, E. Lindahl, *Softwarex* **2015**, 1-2, 19.
10. T. Lu, F. Chen, *J. Comput. Chem.* **2012**, 33, 580.